Chinese Chemical Letters 37 (2026) 112363

Contents lists available at ScienceDirect

Chinese Chemical Letters

journal homepage: www.elsevier.com/locate/cclet

Co d-band center tuning *via* $CoSeO_3$/AlO(OH) heterostructures fabrication to accelerate catalysis and adsorption for enhanced electrochemical sensing towards *ortho*-nitrophenol

Haoran Li[a,1], Huan Xu[a,1], Zhongliao Wang[a], Guanhua Li[a], Ziyi Zheng[a], Shanshan Li[a,*], Qinzhuang Liu[a,*], Xiaofeng Wu[b,*]

[a] Anhui Province Industrial Generic Technology Research Center for Alumics Materials, Anhui Province Key Laboratory of Intelligent Computing and Applications, College of Physics and Electronic Engineering, Huaibei Normal University, Huaibei 235000, China
[b] State Key Laboratory of Digital Medical Engineering, School of Biological Science and Medical Engineering, Southeast University, Nanjing 210096, China

ARTICLE INFO

Article history:
Received 15 July 2025
Revised 28 December 2025
Accepted 4 January 2026
Available online 6 January 2026

Keywords:
$CoSeO_3$/ALO(OH) heterojunction
ONP electrochemical detection
Electronic configuration engineering
Modulation of d-band center
Catalysis and adsorption

ABSTRACT

The development of highly sensitive electrocatalysts for the electrochemical detection of *ortho*-nitrophenol (ONP) is critical for environmental monitoring due to its high toxicity in water environment. Herein, a novel electronic configuration engineering on $CoSeO_3$/AlO(OH) heterostructure with precisely modulated d-band centers is successfully designed. Crucially, a negative shift in the d-band center enhances the catalysis and adsorption ability of the heterostructure. Benefiting from the electron transfer behavior from AlO(OH) to $CoSeO_3$, the electrocatalyst exhibits exceptional ONP sensing performance, achieving an ultrahigh sensitivity of 0.499 μA L μmol^{-1} and a record-low detection limit of 5.353 nmol/L. Furthermore, the experimental characterizations and density functional theory (DFT) calculations reveal that the heterostructure-induced d-band center downshifting optimizes the adsorption strength of ONP, further accelerating the electrochemical redox kinetics. The $CoSeO_3$/AlO(OH) also demonstrates good stability, anti-interference capabilities, and successful application in detecting ONP in real water samples. This study offers a promising strategy for designing advanced electrochemical sensors through heterointerface-based electronic structure engineering.

© 2026 Published by Elsevier B.V. on behalf of Chinese Chemical Society and Institute of Materia Medica, Chinese Academy of Medical Sciences.

Ortho-nitrophenol (ONP) is a significant environmental contaminant commonly found in industrial wastewater, particularly from industries such as petrochemicals, dye manufacturing, and pharmaceuticals [1,2]. Due to its high toxicity [3], the accumulation of ONP poses a potential threat to both ecological systems and human health, making the development of efficient and sensitive methods for the rapid detection of ONP in water crucial [4,5]. Electrochemical sensors are considered ideal for ONP detection due to their simplicity, cost-effectiveness, speed and convenience, coupled with their ability for real-time monitoring [6–9]. Nanomaterials have been widely employed in electrochemical sensors due to their large surface area and favorable electron transport properties, which help improve the detection performance for various pollutants [10,11]. Despite their notable electrochemical performance, numerous nanomaterials continue to encounter limitations in practical applications due to their poor structural stability and vulnerability to interference under complex aqueous conditions. Furthermore, current understanding of their electrochemical behavior and reaction pathways remains limited, offering insufficient theoretical support for rational material design. Therefore, the development of more stable materials and in-depth investigation into their electrochemical mechanisms are essential for advancing the overall performance of electrochemical sensing systems.

Tuning the electronic structure is widely regarded as one of the key strategies for enhancing the performance of functional materials [12]. By manipulating parameters such as particle size, morphology, composition and surface chemistry, it is possible to significantly improve a material's electrical conductivity [13], optical behavior [14], and catalytic activity [15]. At the core of this approach lies the ability to modulate the electronic band structure, carrier distribution, and interfacial charge transfer characteristics, which in turn influence the adsorption behavior of reactants and the kinetics of surface reactions. For instance, Luo *et al.* demonstrated that tailoring the electronic structure of Mn-N active sites could effectively enhance the adsorption affinity for oxygen inter-

* Corresponding authors.
E-mail addresses: sa157002@mail.ustc.edu.cn (S. Li), qzliu@mail.ustc.edu.cn (Q. Liu), wuxiaofeng@seu.edu.cn (X. Wu).
[1] These authors contributed equally to this work.

https://doi.org/10.1016/j.cclet.2026.112363
1001-8417/© 2026 Published by Elsevier B.V. on behalf of Chinese Chemical Society and Institute of Materia Medica, Chinese Academy of Medical Sciences.

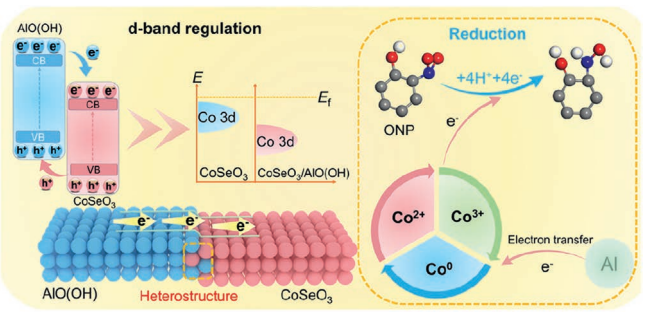
mediates [16]. Notably, among various modulation methods, adjusting the d-band center of transition metals is particularly crucial, as it directly affects the binding strength between active sites and reactants-thus enabling precise control over catalytic activity [17]. For example, the team led by Yu introduced heteroatoms into porous carbon nanofibers to fine-tune the d-band center of Ni sites, thereby optimizing their interaction with reaction intermediates and improving catalytic efficiency in water-splitting reactions [18]. These findings underscore the key role of electronic structure regulation in advancing catalytic performance. In addition, d-band center modulation is increasingly seen as a promising direction within electronic structure engineering, especially for the development of high-efficiency electrocatalytic and sensing materials.

Tuning the d-band center is an effective strategy to regulate the adsorption strength between catalysts and reaction intermediates, thereby optimizing reaction pathways, lowering energy barriers, and improving both catalytic selectivity and reaction kinetics [19,20]. Common approaches for d-band modulation include stress engineering, heteroatom doping, defect introduction and so on [21,22]. For instance, Li *et al.* constructed a Fe_3O_4/La_2O_3 heterostructure by incorporating La_2O_3, which successfully downshifted the d-band center of Fe sites [23]. This adjustment weakened the excessive adsorption of oxygen intermediates and significantly enhanced the oxygen reduction reaction performance. In a different case, Pei *et al.* introduced A-site defects and oxygen vacancies into perovskite-type catalysts, which adjusted the catalyst's d-band center, thereby facilitating the generation of Fe(IV)=O species [24]. This process effectively activated peroxymonosulfate, resulting in enhanced degradation efficiency of levofloxacin. In addition, Shi *et al.* prepared defect-rich copper nanoparticles as catalysts for the hydrogen evolution reaction (HER) using electric discharge in liquid technology. These nanoparticles exhibited excellent catalytic performance across the full pH range, with their remarkable catalytic activity attributed to the enhancement of the copper d-band center by the defects, which improved hydrogen adsorption and water dissociation efficiency [25]. Among the various strategies, constructing heterostructures has emerged as a particularly promising method. It can induce electronic redistribution at the interface and promote asymmetric charge distribution *via* band alignment and electron transfer, ultimately altering the energy level structure of active metal d-orbitals. For example, Li *et al.* synthesized a MoO_3/Ni-NiO heterojunction *via* electrodeposition, which demonstrated outstanding bifunctional catalytic activity for both hydrogen and oxygen evolution reactions [26]. In this system, MoO_3 favored oxygen evolution, while the synergistic effect of the heterojunction enhanced hydrogen evolution performance. In another example, Shen *et al.* designed a crystalline-amorphous $CoSe_2$/CoP heterojunction that introduced strong electronic coupling at the interface [27]. This effectively modulated the d-band center of Co sites, reduced hydrogen overadsorption, and resulted in excellent hydrogen evolution activity. However, despite the widespread use of d-band center modulation in catalytic processes such as HER and oxygen evolution reaction (OER), its application in electrochemical sensing remains relatively underexplored-particularly in the context of detecting organic pollutants like ONP, where relevant studies are still limited.

Transition metal cobalt (Co) has attracted considerable attention in the fields of electrocatalysis and electrochemical sensing due to its tunable d-band center and variable valence states [28]. Co-based materials exhibit versatile electronic configurations, which allow for the modulation of surface electron distribution through valence-state transitions and orbital reconstruction. This, in turn, optimizes the adsorption and activation of reaction intermediates [29]. Studies have shown that incorporating Co not only enhances electrical conductivity and charge transfer efficiency, but also facilitates interfacial reaction kinetics through the formation of multivalent synergistic systems [30]. For instance, Wang *et al.* achieved significant modulation of the electronic structure by doping Co_3O_4 nanosheets with non-metallic sulfur atoms [31]. This approach increased the Co^{2+}/Co^{3+} ratio and introduced a large number of oxygen vacancies. As a result, the reducibility of Co sites was enhanced, and the surface affinity toward pollutant molecules was improved, effectively promoting electron transfer and enabling highly sensitive detection of *p*-nitrophenol. Building on these findings, the construction of heterostructures based on Co compounds has emerged as a promising strategy for further enhancing functional performance. $CoSeO_3$, known for its low lattice energy, high reactivity, and excellent conductivity, has been widely studied for catalytic and sensing applications. Its intrinsic electronic structure facilitates interfacial charge transfer and helps optimize reaction pathways [32]. In combination, AlO(OH) serves as a chemically stable co-component that can regulate the acid-base characteristics and electron density of the composite system. Moreover, it contributes to structural stability and improved exposure of active sites, thereby accelerating electrochemical reaction rates and enhancing selectivity [33].

In this study, a $CoSeO_3$/AlO(OH) heterostructure was designed to modulate the d-band center of Co, achieving excellent electrochemical performance in the detection of ONP. The formation of this heterojunction not only enhanced the material's electron transfer capability but also improved its catalytic and adsorption properties. As a result, the $CoSeO_3$/AlO(OH) composite demonstrated a high sensitivity of 0.499 μA L $μmol^{-1}$ and a low detection limit of 5.353 nmol/L for ONP sensing. Comprehensive characterizations, including X-ray photoelectron spectroscopy (XPS), ultraviolet photoelectron spectroscopy (UPS), and density functional theory (DFT) calculations, were employed to investigate the influence of the heterostructure on electronic properties. The results revealed that AlO(OH), acting as an electron donor, effectively altered the oxidation state of Co by increasing the proportion of highly active Co^{2+} ions and facilitating the $Co^0/Co^{2+}/Co^{3+}$ redox cycle. This electron redistribution significantly enhanced the redox reaction of ONP. Moreover, the $CoSeO_3$/AlO(OH) composite exhibited good stability and anti-interference capability, proving effective in the detection of ONP in real water samples.

We first synthesized the $CoSeO_3$/AlO(OH) heterostructure *via* a facile two-step strategy. This synthetic route enabled the intimate integration of $CoSeO_3$ nanosheets with AlO(OH), forming a well-defined heterojunction interface. As shown in Scheme 1, the electronic structure of $CoSeO_3$ was modulated after the formation of the $CoSeO_3$/AlO(OH) heterojunction, particularly through the downshifting of the d-band center, significantly enhancing its catalytic and adsorption properties. The downshifted d-band center optimized the interaction between the Co d-orbitals and the reactant ONP, lowering the energy barrier for the reaction and improv-



Scheme 1. A method for ONP detection using $CoSeO_3$/AlO(OH) nanosheets, where the modulation of the Co d-band center *via* heterostructure construction accelerates catalytic and adsorption enhancement.

ing electrochemical reaction kinetics. Specifically, AlO(OH) donates electrons to $CoSeO_3$, reducing Co^{3+} to Co^{2+} and further to Co^0, thereby altering the oxidation state of Co. This adjustment in the d-band center promotes the $Co^0/Co^{2+}/Co^{3+}$ redox cycle, increasing the proportion of Co^0 and enhancing its role as an effective electron donor. Additionally, the local changes in electron transfer and the optimization of the surface electron density effectively enhanced the adsorption capacity and reduction of $CoSeO_3$/AlO(OH) towards ONP. The redistribution of electrons at the interface and the improved carrier concentration facilitated charge separation and migration, further enhancing the electrochemical sensing performance.

The schematic representation of the synthesis process for $CoSeO_3$/AlO(OH) nanosheets is provided in Fig. 1a. Figs. 1b-d present the scanning electron microscopy (SEM) and transmission electron microscopy (TEM) images of $CoSeO_3$/AlO(OH), which reveal that the sample consists of hexagonal nanosheet with dimensions ranging from 600 nm to 800 nm and the edge-specific growth of nanoflowers. In addition, the nanosheets possess ultrathin thickness, rendering them nearly electron-transparent under both SEM and TEM observation. Such structural features endow the nanosheets with abundant exposed active sites, which contributes to higher reaction rates and catalytic efficiency [34]. As shown in Figs. 1e-g, the red dashed lines clearly delineate the interfacial regions between $CoSeO_3$ and AlO(OH), revealing distinct features indicative of typical hetero-face. This result effectively demonstrates the successful construction of $CoSeO_3$ and AlO(OH) into a heterojunction interface. Figs. 1h-k and Fig. S3 (Supporting information) show the energy dispersive spectroscopy (EDS) elemental maps and spectra of $CoSeO_3$/AlO(OH), indicating that $CoSeO_3$ and AlO(OH) are successfully complexed together with a uniform distribution. In contrast to the pure materials ($CoSeO_3$ and AlO(OH), Figs. S1 and S2 in Supporting information), the morphology of $CoSeO_3$/AlO(OH) demonstrates markedly different morphological characteristics, revealing that the incorporation of Co or Al substantially alters the material's morphology.

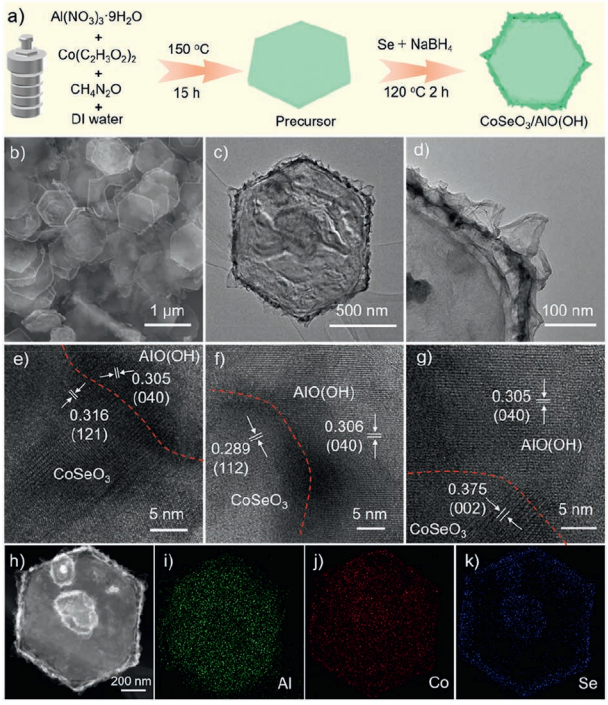


Fig. 1. (a) Scheme for synthesizing $CoSeO_3$/AlO(OH) nanosheets. (b) SEM images, (c, d) TEM images, (e-g) HRTEM images and (h-k) EDS elemental mapping images of $CoSeO_3$/AlO(OH).

The X-ray diffraction (XRD) patterns in Fig. 2a match well with the standard spectra of $CoSeO_3$ (JCPDS No. 80–1391) and AlO(OH) (JCPDS No. 88–2112), respectively. The presence of both $CoSeO_3$ and AlO(OH) peaks in the XRD pattern of the $CoSeO_3$/AlO(OH) composite confirms the successful fabrication of $CoSeO_3$/AlO(OH) nanosheets. As depicted in Fig. 2b, the UPS measurements were carried out to investigate the energy band structure and electronic states of the samples, which reveal the work functions of 6.72 eV and 5.41 eV for $CoSeO_3$ and AlO(OH), respectively. AlO(OH) exhibits the lowest work function among the materials involved, indicating a higher tendency to donate electrons. In contrast, $CoSeO_3$ possesses a comparatively higher work function, making it more likely to accept electrons during the charge transfer process. As a result, when the two materials form a heterostructure, leading to a redistribution of charge at the interface. This electron transfer is not only energetically favorable but also facilitates subsequent charge transport and catalytic reactions [35,36]. The density of states (DOS) for $CoSeO_3$ and $CoSeO_3$/AlO(OH) (Fig. 2c) further shows that, during the heterojunction formation, the d-band shifts downward (Fig. 2d), which can be attributed to the electron donation from Al to Co, resulting in the creation of a distinct complex electronic state [37]. As known, the shift of d-band center will adjust the interaction between the adsorbate and materials, as well as the carrier concentration, which will affect the adsorption and conductivity of the materials [22,38]. As a result, tuning the position of the d-band center plays a crucial role in enhancing the catalytic performance of the material [39,40].

The ultraviolet-visible (UV–vis) spectroscopy and Tauc plot analysis (Fig. S4 in Supporting information, Tauc exponent = 1/2) demonstrate that, $CoSeO_3$ with its narrow band gap of 1.52 eV offers good electrical conductivity, while AlO(OH), having a wider band gap of 4.30 eV, demonstrates excellent insulating properties and structural stability. When these two materials form a composite heterostructure, their differing band gaps lead to a realignment of energy levels, resulting in an effective band offset at the interface. This energy-level alignment provides a potential driving force for electron transfer from AlO(OH) to $CoSeO_3$ at the interface [41,42]. Further analysis, in conjunction with the energy band structure shown in Fig. 2e, reveals that the two materials form a typical heterojunction. Specifically, the conduction band minimum (CBM) of AlO(OH) is −1.67 eV, which is higher than that of $CoSeO_3$ at −5.46 eV, allowing electrons to transfer from AlO(OH) to $CoSeO_3$. Conversely, the valence band maximum (VBM) of AlO(OH) is −5.97 eV, which is higher than that of $CoSeO_3$ at −6.98 eV, enabling holes to move from $CoSeO_3$ to AlO(OH). Upon heterojunction formation, the CBM and VBM shift, promoting efficient electron transfer at the interface. This energy level alignment demonstrates that the heterojunctions enhance charge separation, improving electrochemical performance by adjusting the d-band center. These electronic behaviors significantly boost the performance of the composite materials in electrochemical detection, as evidenced by their high sensitivity, selectivity, and exceptional charge transport capability. Moreover, this modulation of the energy bands and optimization of the interface considerably reduce interfacial resistance, leading to faster electrical signal responses.

Fig. 2f presents the XPS spectra of Co 2p before and after the material compositing. The peaks at 784.9 eV and 802.0 eV are attributed to Co^{2+}, while the peaks at 778.3 eV and 793.2 eV correspond to Co^0 [43], which are recognized as the active components of cobaltides. The peaks observed at 781.6 eV and 797 eV are related to Co^{3+}. Following the composite formation, the Co peaks shift to lower binding energies, and Co^0 is generated. This suggests that the Co element gains electrons after the formation of the composite, leading to the reduction of Co^{3+} to Co^{2+} and Co^{2+} to Co^0. Similarly, an increase binding energy of Al 2p (Fig. 2g) indicates Al loses electrons in the composite, acting as an elec-

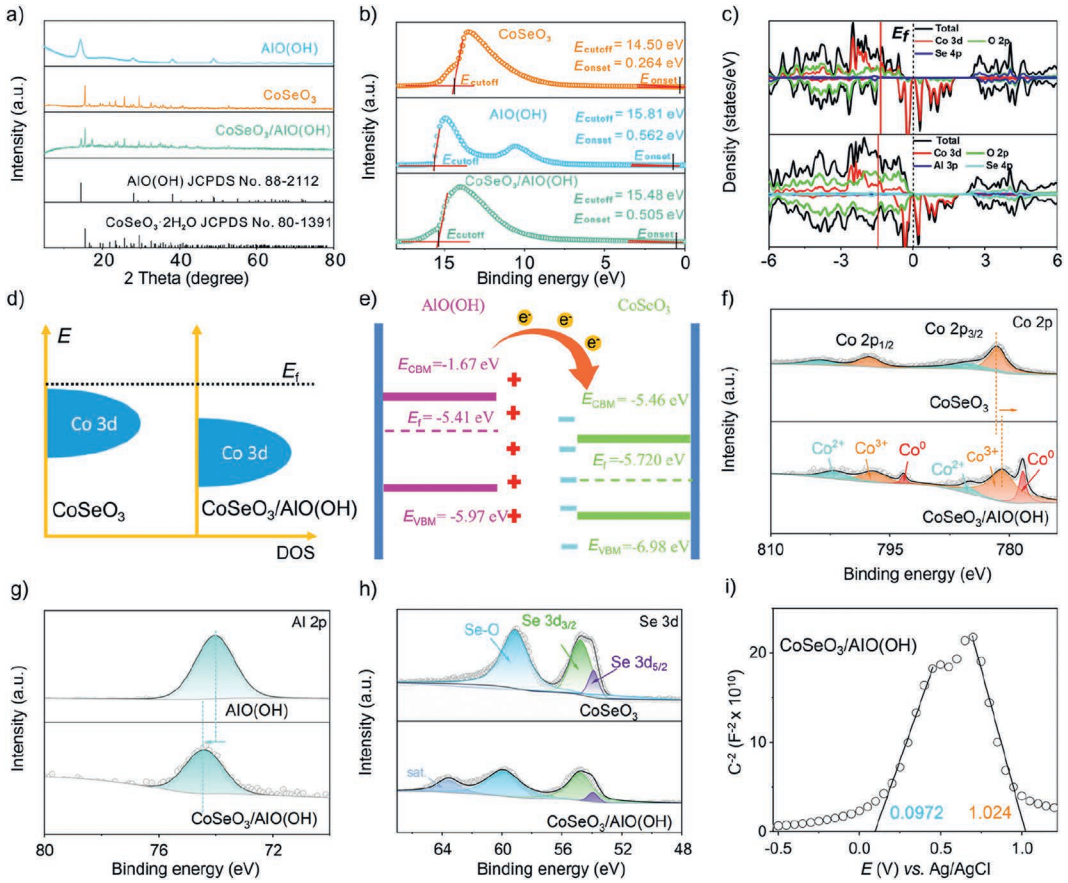


Fig. 2. (a) XRD pattern and (b) UPS of $CoSeO_3$, AlO(OH) and $CoSeO_3$/AlO(OH). (c) The density of states for $CoSeO_3$ and $CoSeO_3$/AlO(OH). (d) Schematic diagram of the Co 3d band structure. (e) Schematic diagram of electron transfer and the corresponding energy band diagram of $CoSeO_3$ and AlO(OH). The XPS spectra of (f) Co 2p, (g) Al 2p and (h) Se 3d of $CoSeO_3$, AlO(OH) and $CoSeO_3$/AlO(OH). (i) Mott-Schottky curves of $CoSeO_3$/AlO(OH).

tron donor after complexation [44]. Additionally, the binding energy of Se in $CoSeO_3$/AlO(OH) remains consistent with that in the $CoSeO_3$/AlO(OH) composite (Fig. 2h), indicating that the chemical state of Se remains stable and unaffected in the composite. All these findings suggest that when the $CoSeO_3$ and AlO(OH) get together, the electron will transfer from AlO(OH) to $CoSeO_3$ and promote the conversion of Co^{3+} to Co^{2+} and Co^{2+} to Co^0. This result is completely consistent with the above characterization results (*i.e.* UPS, DOS and UV–vis), once again demonstrating the abundant electron transfer at the heterojunction interface. Fig. 2i show the Mott-Schottky curve for the $CoSeO_3$/AlO(OH) heterojunction. The positive slope of the curve confirms that the material is an n-type semiconductor. According to the Mott-Schottky relation: $1/C^2 = 2(V\text{-}E_{fb}\text{-}kT/e)/(\varepsilon\varepsilon_0 eN_D)$. V is the applied potential, E_{fb} is the flat-band potential (1.024 for $CoSeO_3$, 0.097 for AlO(OH)), ε is the dielectric constant of the semiconductor (~120 for $CoSeO_3$ and ~6 for AlO(OH)), ε_0 is the vacuum permittivity (8.85×10^{-12} F/m), N_D is the charge carrier density and e is the elementary charge (1.602×10^{-19}C) [45–48]. From the intercept of the linear portion of the $1/C^2$-V curve, we extract E_{fb} and report it in volts (V). For $CoSeO_3$, the slope of the intercept is 8.77. For AlO(OH), the slope of the intercept is 3.79. The figure shows carrier densities of 1.34×10^{18} cm^{-3} for $CoSeO_3$ and 6.20×10^{19} cm^{-3} for AlO(OH), indicating the presence of high charge transfer capacity in the heterojunction. Furthermore, the Mott-Schottky test demonstrates that the efficiency of charge transfer and transport is significantly improved under the influence of an applied electric field. The comprehensive analysis of the energy level distributions and interfacial electronic behavior of $CoSeO_3$, AlO(OH) and their heterojunction $CoSeO_3$/AlO(OH) will offer valuable insights into the mechanisms behind their enhanced performance in electrochemical detection.

The electrochemical redox properties of ONP on $CoSeO_3$, AlO(OH) and $CoSeO_3$/AlO(OH) were investigated. These electrodes were used for the detection of trace ONP using the differential pulse voltammetry (DPV) technique under optimized electrochemical conditions. Typically, a 0.1 mol/L PBS solution (pH 6.0) was used as the electrolyte, with the deposition potential and deposition time set at 0.2 V and 90 s, respectively, and a modified concentration of 1.5 mg/mL. Based on cyclic voltammograms (CV) and electrochemical impedance spectroscopy (EIS), the electrochemical conductivity of $CoSeO_3$/AlO(OH) was higher than that of $CoSeO_3$ and AlO(OH) (Fig. S6 in Supporting information). The electrochemical surface areas were determined from the double-layer capacitance values (Fig. S7 in Supporting information) and calculated to be 0.0455 cm^2 for $CoSeO_3$, 0.0394 cm^2 for AlO(OH), and 0.0503 cm^2 for $CoSeO_3$/AlO(OH). Considering the geometric area of the glassy carbon electrode (0.076 cm^2), the percentage of electrochemically active surface area is 59.9 %, 51.8 %, and 66.2 % for $CoSeO_3$, AlO(OH), and $CoSeO_3$/AlO(OH), respectively. These results clearly demonstrate that the heterostructure increases the effective utilization of the electrode surface, thereby supplying more active sites for ONP reduction and enhancing the sensitivity of the sensor.

In order to investigate the effect of $CoSeO_3$/AlO(OH) on electron transfer, a study was carried out by CV. As shown in Fig. 3a, in PBS solution containing 300 μmol/L ONP, all electrodes exhibited an irreversible reduction peak at −0.654 V (R_1), among which the redox peak current of the $CoSeO_3$/AlO(OH) GCE was significantly higher than that of the other electrodes, indicating that it

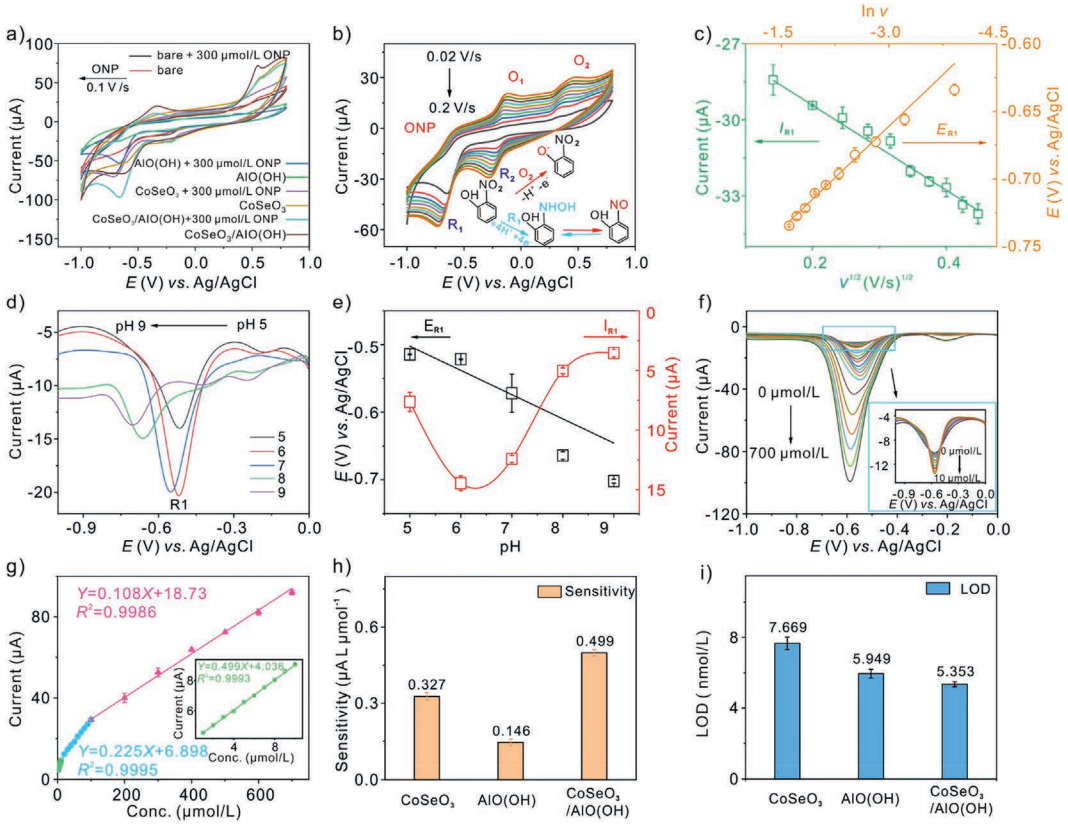


Fig. 3. (a) CV curves of bare, $CoSeO_3$, AlO(OH) and $CoSeO_3$/AlO(OH) modified GCEs at a scan rate of 0.1 V/s with and without 300 μmol/L ONP in 0.1 mol/L PBS (pH 6.0). (b) CV curves of 300 μmol/L ONP on $CoSeO_3$/AlO(OH) GCE with different scan rates (0.02–0.2 V/s). (c) Plots of I_{R1} *vs.* $\nu^{1/2}$ and E_{R1} *vs.* ln ν for ONP. (d) DPV curves of 100 μmol/L of ONP on $CoSeO_3$/AlO(OH) GCE in 0.1 mol/L PBS with different pH values. (e) Plots I_{R1} and E_{R1} *vs.* pH for ONP. (f) DPV of $CoSeO_3$/AlO(OH) GCE with the working dynamic range of ONP from 0 μmol/L to 700 μmol/L in 0.1 mol/L PBS (pH 6.0). (g) The DPV curve and a concentration calibration curve of ONP. Inset correspond to a partial magnification of ONP at low working dynamic range (0–10 μmol/L). (h, i) Comparison of sensitivities and LOD for the DPV detection of ONP on $CoSeO_3$, AlO(OH) and $CoSeO_3$/AlO(OH) GCEs. Error bars correspond to standard deviations of three independent measurements.

possesses a higher electron transfer capacity and more catalytically active sites [49]. In addition, the $CoSeO_3$/AlO(OH) GCE exhibited a significant enhancement of the peak current and a tendency for the peak potential R_1 to move toward the cathode when the scanning rate was increased, which was consistent with the irreversible kinetic characteristics [50], further confirming its superior electrochemical catalytic performance and reactivity.

The effect of scan rate (0.02–0.2 V/s) on the $CoSeO_3$/AlO(OH) redox peak current and potential on ONP is investigated in Figs. 3b and c. The peak current increased with the scan rate (Fig. 3b). For the irreversible wave (R1) of the ONP, the peak potential shifted towards the cathode with increasing scan rate, which is in accordance with Nicholson's theory of irreversible kinetics [50]. As shown in Fig. 3c. Both reversible or irreversible redox peak currents are linearly related to the square root of the scan rate. This indicates that the reactions of ONP on the $CoSeO_3$/AlO(OH) GCE surface are all diffusion-controlled processes. In order to avoid the interference of the background current and obtain clear spikes, a scan rate of 0.1 V/s was chosen for the subsequent electrochemical detection. Meanwhile, it can be observed that the reduction potential E_{R1} of ONP (Fig. 3c) is negatively correlated with the natural logarithm of the scan rate (lnν). The linear equation between E and ln ν can be written as follows:

$$E_{R1}(\text{ONP})/\text{V} = -0.0507\ \ln(\nu/(\text{V/s}))\ -\ 0.8131\ (R^2 = 0.9663) \quad (1)$$

$$I_{R1}(\text{ONP})/\mu\text{A} = -16.7875\ (\nu/(\text{V/s}))\ -\ 26.0674\ (R^2 = 0.9903) \quad (2)$$

With the increase of pH from 5.0 to 9.0 (Figs. 3d-e), the reduction peak potential and current of ONP changed significantly, indicating that pH has an important effect on the reaction process. According to the formula $E_R = E^0$ - (0.059m/n)pH, the ratio of protons (m) to electrons (n) in the reaction is about 2:3 [51]. Although the stoichiometric proton-to-electron ratio (m:n = 2:3) suggests that electron participation is prominent, such information by itself does not fully capture the reaction dynamics. A more comprehensive interpretation emerges when kinetic and interfacial factors are considered. The $CoSeO_3$/AlO(OH) heterostructure exhibits a markedly reduced charge-transfer resistance, indicating that electron migration across the interface is significantly facilitated [52]. Meanwhile, DFT calculations confirm that ONP molecules adsorb more favorably at the heterointerface, lowering the activation barrier for subsequent electron-driven steps. Furthermore, the dependence of peak parameters on scan rate and pH is consistent with a proton-coupled electron transfer process, where proton avail ability influences–but does not solely dictate-the overall kinetics [53]. Taken together, these findings support a mechanism in which interfacial electron transfer is strongly enhanced by heterostructure engineering, while protons act in concert to sustain the redox cycle. It was found that the reduction peak current of ONP reached its maximum value at pH 6.0, indicating that this pH is the optimum condition for the redox of ONP. This is due to the fact that $CoSeO_3$/AlO(OH) is unstable under acidic conditions, and higher pH will weaken the complementary protonation process of ONP redox [54]. Therefore, pH 6.0 was determined to be the optimal condition for the measurement.

After optimizing the detection conditions, we further explored the DPV response to ONP in the low (0–10 μmol/L), medium (10–100 μmol/L) and high (100–700 μmol/L) operating dynamic ranges for the three samples. ONP was detected by $CoSeO_3$/AlO(OH) GCE (Figs. 3f and g) and compared with $CoSeO_3$ and AlO(OH) (Figs. S8a-d in Supporting information). $CoSeO_3$/AlO(OH) showed a clear DPV response to 0–700 μmol/L ONP. The sensitivities of $CoSeO_3$/AlO(OH) GCE at 0–10 μmol/L, 10–100 μmol/L, and 100–700 μmol/L ONP are 0.499, 0.225, and 0.108 μA L μmol^{-1}. A detection limit of 5.353 nmol/L was calculated based on the conventional $3\sigma/k$ approach, in which σ denotes the standard deviation of the blank measurements and k corresponds to the slope of the calibration curve at lower concentration levels [55,56]. Segmentation results showed that the sensitivity of ONP decreased with increasing concentration, which may be due to the adsorption saturation of ONP on nanomaterials at high concentrations. The modest shift in the DPV peak potential with increasing analyte concentration can be explained by the surface accumulation of reaction intermediates and concurrent changes in mass transport pathways and interfacial properties, leading to minor adjustments of the electrode's surface potential [57,58]. The sensitivities and LOD of $CoSeO_3$, AlO(OH) and $CoSeO_3$/AlO(OH) GCE to ONP at low concentrations are visualized and compared in the histograms of Figs. 3h and i. The results showed that $CoSeO_3$/AlO(OH) had the best performance for the detection of ONP. An obvious enhancement of electrochemical performance of $CoSeO_3$/AlO(OH) is found when compared to single $CoSeO_3$ or AlO(OH), indicating the useful modulation of electroanalysis performance by the formation of heterojunction. The sensitivity and LOD of $CoSeO_3$/AlO(OH) GCE in ONP detection were also compared with other materials in previous works (Table S1 in Supporting information), and the results showed that $CoSeO_3$/AlO(OH) had superior performance in DPV detection. These results demonstrate the potential of $CoSeO_3$/AlO(OH) for practical applications in electrochemical detection. To further explore the reason for the excellent electrochemical performance of $CoSeO_3$/AlO(OH), the superiority of $CoSeO_3$/AlO(OH) for ONP detection was further analyzed in terms of both adsorption and catalysis.

From an electronic perspective of DFT calculations, the electron transfer of $CoSeO_3$ towards the target molecule ONP is 0.06 e, while for the $CoSeO_3$/AlO(OH) heterojunction is 0.08 e (Figs. 4a-c and Fig. S9 in Supporting information), indicating an increased electron transfer ability in heterojunction interface. The adsorption energy of $CoSeO_3$ towards ONP is −0.80 eV, while for the $CoSeO_3$/AlO(OH) heterojunction is −0.96 eV (Table S2 in Supporting information), suggesting that the heterojunction has stronger adsorption ability than that of $CoSeO_3$. It means that when the heterojunction adsorbs ONP, the electron will shift to ONP, which will facilitate the reduction of ONP and thereby lead to an increased reduction current during the detection [22,33]. It is because that an electron-rich state and enhanced surface electronic activity can be formed on $CoSeO_3$ in $CoSeO_3$/AlO(OH) heterojunction, resulting from the electron transfer from the AlO(OH) region to the $CoSeO_3$ region as proved above. The presence of such an electron-rich state is critical for the subsequent adsorption and electrochemical redox of ONP. In a word, the heterojunction interface establishes a stable electron transport pathway, promoting efficient directional electron flow from AlO(OH) through $CoSeO_3$ to ONP. This redistribution of electrons not only optimizes the interfacial electronic structure of the composite but also significantly improves the recognition and catalytic efficiency toward ONP. By acting as an electron donor, AlO(OH) effectively regulates the d-orbital electron configuration of $CoSeO_3$, thereby creating a more favorable electronic environment for the electrochemical detection of ONP. These findings suggest that the interfacial electron behavior induced by constructing the AlO(OH)/$CoSeO_3$ heterostructure plays a crucial role in achieving high sensitivity and enhanced catalytic performance of the material [52,53]. The adsorption capacity of the synthesized materials was comprehensively validated through systematic sorption-diffusion investigations using ultraviolet absorption spectra (Fig. 4d). Detailed analyses were conducted to examine the contaminant uptake patterns across varying concentrations (10, 100, and 400 μmol/L ONP) on $CoSeO_3$, AlO(OH) and $CoSeO_3$/AlO(OH). Experimental findings consistently demonstrated hierarchical removal efficiency among the tested materials, with $CoSeO_3$/AlO(OH) exhibiting superior performance compared to both individual components ($CoSeO_3$ and AlO(OH)) across all tested concentrations (Fig. 4e). Notably, the composite material achieved optimal contaminant removal at 100 μmol/L concentration, where maximum adsorption equilibrium was attained. This concentration-dependent behavior suggests enhanced synergistic interactions within the hybrid material's structure during the adsorption process [51]. The observed concentration-dependent behavior aligns with the variable sensitivity profile of $CoSeO_3$/AlO(OH) across different concentration regimes. To further systematically evaluate the reduction-diffusion characteristics of $CoSeO_3$/AlO(OH)-modified GCE in phosphate-buffered saline (PBS, pH 6.0), chronoamperometric analyses were conducted across ONP concentrations spanning 0–400 μmol/L (Fig. 4g and Fig. S10 in Supporting information). The composite-modified electrode exhibited linear current dependence on the inverse square root of time ($t^{-1/2}$), as evidenced by the inset calibration curve. Through application of the Cottrell equation:

$$I_p = nFAC_0D^{1/2}\pi^{-1/2}t^{-1/2} \quad (3)$$

where n denotes electron transfer stoichiometry, F represents Faraday's constant, A indicates electrode surface area, C_0 corresponds to analyte concentration, t signifies elapsed time, and the diffusion coefficient (D) [59] for $CoSeO_3$/AlO(OH) was calculated as 1.939×10^{-6} m^2/s. Comparative analysis of D values (Fig. 4h) revealed superior mass transport characteristics in the composite material, with greater ONP uptake than its individual counterparts. This enhanced diffusivity correlates with improved electrochemical reaction probability and signal amplification, as established in prior studies where D values directly govern interfacial analyte transport kinetics [60]. This correlation further rationalizes the DPV response hierarchy observed among the materials, confirming the critical role of coupled adsorption-diffusion processes in ONP sensing. The systematic validation through both equilibrium adsorption studies and dynamic electrochemical measurements reinforces the experimental methodology's robustness.

XPS analyses of Co after adsorption with ONP on $CoSeO_3$/AlO(OH) were scrutinized to further explore potential adsorption mechanisms (Fig. 4f). As mentioned earlier, Al provides electrons to reduce Co^{3+} to Co^{2+} and Co^{2+} to Co^0 in $CoSeO_3$, as the complexation of Al and Co may lead to a local change in the electron density, which facilitates the flow of electrons. This leads to an increase in the $Co^0/Co^{2+}/Co^{3+}$ ratio, generating an excellent electron donor in the form of Co^0 and potentially accelerating the Co^{2+}/Co^{3+} cycle [43,61–63]. The valence state of Co in $CoSeO_3$/AlO(OH) changed after physisorption of ONP compared to the pure sample (Fig. 4f). This shows the electron transfer between the heterojunction of $CoSeO_3$/AlO(OH) and ONP. The adsorption of ONP resulted in a slight decrease in the Co^0 content. In this case, the heterojunction provides a bridge for electron transfer from $CoSeO_3$, where Co^0 is oxidized to Co^{2+} and Co^{3+} and the excess electrons are supplied to the organic pollutant, ONP, to promote catalyst of ONP. The significant change in Co valence state further suggests that Co species (*i.e.*, $Co^0/Co^{2+}/Co^{3+}$ cycles) are the key active sites for redox ONP. Overall, the improved activity of the $CoSeO_3$/AlO(OH) heterostructure arises from the cooperative cycling of Co^{3+}, Co^{2+}, and Co^0. Co^{3+} accepts electrons from the

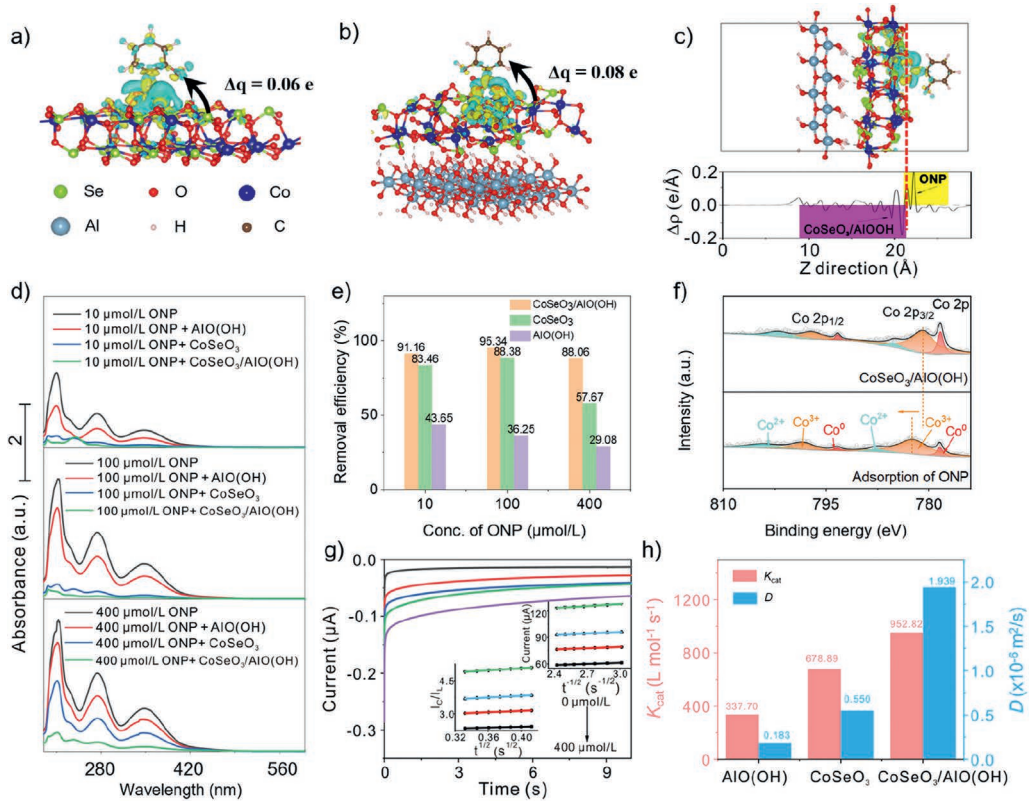


Fig. 4. Side view of the charge density difference of (a) $CoSeO_3$ and (b) $CoSeO_3$/AlO(OH) adsorbed with ONP with an isosurface of 1.5×10^{-3} e/Å^3. The charge accumulation is shown as the yellow region, and the charge depletion is shown as the cyan region. (c) Planar-averaged electron density difference $\Delta\rho(z)$ for $CoSeO_3$/AlO(OH) adsorbed with ONP. The yellow and cyan areas indicate electron accumulation and depletion, respectively. (d) Ultraviolet absorption spectra of $CoSeO_3$/AlO(OH) to 10, 100 and 400 μmol/L ONP. (e) ONP removal efficiency by $CoSeO_3$, AlO(OH) and $CoSeO_3$/AlO(OH). High-resolution XPS spectra of (f) Co 2p for $CoSeO_3$/AlO(OH) after physical adsorption with 100 μmol/L ONP. (g) Chronoamperograms obtained at $CoSeO_3$/AlO(OH) GCE in PBS for ONP concentrations of 0, 200, 400, 600 and 800 μmol/L. Insets: plots of I *vs.* $t^{-1/2}$ and I_C/I_L on $t^{1/2}$ obtained from chronoamperometry. (h) D and K_{cat} calculated by Chronoamperograms of $CoSeO_3$, AlO(OH) and $CoSeO_3$/AlO(OH).

electrode and is reduced to Co^{2+}, mediating charge transfer to ONP. At more negative potentials, Co^{2+} is further reduced to Co^0, which donates electrons directly to ONP intermediates, accelerating their conversion to aminophenol. This valence relay provides a stable electron reservoir and underpins the enhanced sensitivity observed.

Complementary catalytic investigations were conducted to elucidate the underlying mechanisms governing the observed electrochemical performance. The catalytic rate constant (K_{cat}) for ONP electroreduction was quantitatively determined through chronoamperometric analysis combined with the Gales equation [64]:

$$I_C/I_L = \pi^{1/2}\gamma^{1/2} = \pi^{1/2}(K_{cat}C_0t)^{1/2} \quad (4)$$

where I_C and I_L denote catalytic currents in the presence and absence of ONP, respectively (see inset chronoamperogram). The composite $CoSeO_3$/AlO(OH)-modified electrode demonstrated exceptional catalytic efficiency with K_{cat} value of 952.82 L mol^{-1} s^{-1}, exceeding those of $CoSeO_3$ (678.89 L mol^{-1} s^{-1}) and AlO(OH) (337.70 L mol^{-1} s^{-1}) GCE by approximately 40.4 % and 182.2 %, respectively (Fig. 4h). The results show that the higher the value of *K*, the better the catalytic performance of the material in the electroanalysis. This implies that $CoSeO_3$/AlO(OH) has the best catalytic ability, which is mainly attributed to its best conductivity, the most active center and the excellent electron transfer ability of the heterojunction after composite.

Figs. 5a-d and Fig. S11 (Supporting information) shows that the common organic pollutants (*e.g.*, 3-CNB, PNP, phenol, HQ, *p*-BQ and PYRO) in the aqueous environment has a tendency to interfere the electrochemical detection of ONP. However, most of these interferences are negligible. As shown in Figs. S11b and S12 (Supporting information), we fixed ONP at 100 μmol/L and incrementally spiked phenol (and other co-phenolics) until the ONP peak current deviated by ≤5 % from the value in the absence of interferent. Quantify tolerance ratios (interferent:analyte): phenol:ONP = 3:5, PNP:ONP = 2:1. To minimize signal overlap, we subsequently performed optimization experiments by adjusting both the solution pH and the DPV pulse parameters (including incremental potential, amplitude, pulse width, Fig. S13 in Supporting information). In ONP-PNP mixtures, two peaks are resolved and the separation increases with pH, which can attribute to speciation-driven shifts of nitrophenolate equilibria, enabling reliable ONP quantification. This observations indicate that acid-base control is effective for nitrophenol pairs [65,66]. In contrast, the interference between phenol and ONP displays limited change as the variation of pH/pulse-parameters, and phenol mainly acts as a competitor that occupies active sites. Future work may pay more attention to this problem. In addition, the interference of the common inorganic cations (*e.g.*, K^+, Zn^{2+}, Ag^+, Fe^{3+}, Ni^{2+}) and inorganic anions (*e.g.*, $Cr_2O_7^-$, Cl^-, SO_4^{2-}, NO_3^-, Br^-, CN^-) were tested and showed that these inorganic ions have almost no effect on the ONP detection (Figs. 5e and f). This indicates that based on the $CoSeO_3$/AlO(OH) GCE, the detection of ONP has good selectivity and anti-interference ability, even for compounds with similar properties to ONP.

Fig. S14 (Supporting information) show that the electrochemical performance of $CoSeO_3$/AlO(OH) GCE has excellent stability. During 20 consecutive electrochemical tests, the measurement results were almost unchanged with a relative standard deviation of only 1.72 %, indicating that the composite-modified electrode

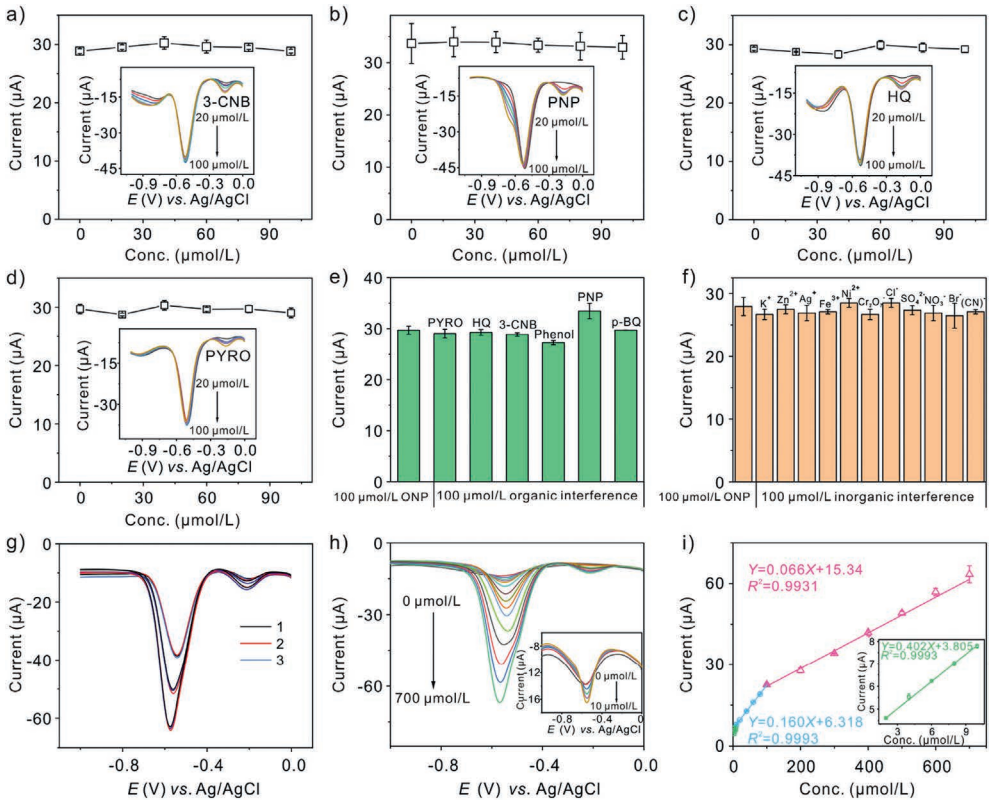


Fig. 5. Interference studies of (a) 3-chloronitrobenzene (3-CNB), (b) *p*-nitrophenol (PNP), (c) hydroquinone (HQ) and (d) pyrocatechol (PYRO) toward 100 μmol/L ONP on $CoSeO_3$/AlO(OH) GCE. Comparison of the (e) organic interference and (f) inorganic interference for PNP detection on $CoSeO_3$/AlO(OH) GCE. (g) DPV respond of 100, 200, 300 μmol/L ONP on three different GCEs with the same modification process to fabricate $CoSeO_3$/AlO(OH) GCE. (h) DPV response of ONP and (i) the corresponding linear calibration of peak current to ONP in real water sample on $CoSeO_3$/AlO(OH) GCE. Insets in *c* and *d* are partial magnification of ONP at low working dynamic range (0–10 μmol/L).

has good stability. In addition, the DPV response results of three newly constructed electrodes (Fig. 5g) and three electrodes stored at room temperature for 10 days (Fig. S15 in Supporting information) to ONP indicated that the currents and shapes of the reduction peaks were basically unchanged. These results demonstrate that the $CoSeO_3$/AlO(OH) GCE are not only highly stable, but also have the potential for reliable detection and long-term use in practical applications.

The detection performance of $CoSeO_3$/AlO(OH) GCE and its practical application were further verified by testing on real water samples. The natural lake water in Huaibei City, Anhui Province, was used as the sample. After the impurities were removed by stirring and centrifugal filtration, the lake water was mixed with 0.1 mol/L PBS (pH 6.0) at the ratio of 1:9 by volume to form the buffer solution for testing (Figs. 5h and i). Experiments showed that the $CoSeO_3$/AlO(OH) GCE was able to sensitively detect ONP in real sample, even though the organic ions in the lake water slightly reduced the detection sensitivity, it still showed excellent performance. The detection sensitivity of the lake water sample was 0.402 μA L $μmol^{-1}$ with a linear correlation coefficient of 0.9993, which was only slightly reduced compared with the pure buffer environment. To further validate the applicability of the sensor in real environments, we performed recovery tests in real water (tap water, lake water and wastewater of Huaibei City) (diluted with PBS) with ONP at three concentration levels (low, medium and high). The recoveries ranged from 93.08 % to 107.58 %, demonstrating reliable quantification across a wide dynamic range (Table S3 in Supporting information). In conclusion, the $CoSeO_3$/AlO(OH) GCE has good accuracy and reliability, showing its great potential for the detection of ONP in real water environments and providing strong support for practical applications.

In summary, we have successfully developed a novel $CoSeO_3$/AlO(OH) heterostructure with precisely modulated electronic properties for highly sensitive and selective detection of toxic ONP. Significantly, the interfacial electron redistribution in the heterostructure resulted in remarkable sensing performance, achieving an ultrahigh sensitivity of 0.499 μA L $μmol^{-1}$ and a record-low detection limit of 5.353 nmol/L, surpassing most previously reported ONP sensors. Comprehensive experimental characterizations and theoretical simulations demonstrate that the downshifted d-band center, induced by asymmetric charge distribution through the AlO(OH)-mediated electron donation effect, optimizes the adsorption strength for ONP and promotes efficient electrochemical redox kinetics. Moreover, the fabricated sensor exhibited excellent anti-interference capability and long-term stability in real water sample analysis. This study provides a fundamental understanding of electronic structure regulation through heterojunction engineering and offers a promising strategy for designing advanced electrochemical sensors in environmental monitoring applications. The $CoSeO_3$/AlO(OH) heterostructure demonstrates excellent sensitivity and stability for ONP detection. Nevertheless, challenges remain for real-world application, including the long-term durability and anti-interference under environmental conditions, and the scalability of electrode preparation. These aspects warrant further investigation to ensure practical deployment.

Declaration of competing interest

The authors declare that they have no known competing financial interests or personal relationships that could have appeared to influence the work reported in this paper.

CRediT authorship contribution statement

Haoran Li: Writing – original draft, Visualization, Validation, Investigation. **Huan Xu:** Writing – original draft, Investigation. **Zhongliao Wang:** Software, Investigation. **Guanhua Li:** Investigation. **Ziyi Zheng:** Investigation. **Shanshan Li:** Writing – review & editing, Supervision, Project administration, Funding acquisition. **Qinzhuang Liu:** Writing – review & editing, Funding acquisition. **Xiaofeng Wu:** Writing – review & editing, Supervision, Funding acquisition.

Acknowledgments

This research is supported by National Natural Science Foundation of China (Nos. 22406060 and 22407024), the Excellent Scientific Research and Innovation Team of the Education Department of Anhui Province (Nos. 2023AH010043 and 2024AH010027), the Middle-aged and Young Teachers' Training Action Discipline (Major) Leader Cultivation Project, China (No. DTR2023022), Anhui Province Colleges and Universities Young and Middle-aged Teachers' Training Action - Key Project for Cultivating Outstanding Young Teachers (No. YQZD2025039), the Key Natural Science Research Project for Colleges and Universities of Anhui Province (No. 2023AH050340), and National College Students Innovation and Entrepreneurship Training Program of China (No. 202410373031).

Supplementary materials

Supplementary material associated with this article can be found, in the online version, at doi:10.1016/j.cclet.2026.112363.

References

[1] H. Zhan, Q. Zhou, M. Li, et al., Appl. Catal. B: Environ. 310 (2022) 121329.
[2] M. Wang, G. Zhang, S. Dong, et al., Adv. Funct. Mater. 34 (2024) 2406516.
[3] M. Misra, S.R. Chowdhury, T.I. Lee, Appl. Catal. B: Environ. 272 (2020) 118991.
[4] Y. Li, Y. Ma, E. Lichtfouse, et al., J. Hazard. Mater. 421 (2022) 126718.
[5] B. Liu, M. Cai, X. Feng, et al., Carbon 209 (2023) 118003.
[6] X. Li, J. Ping, Y. Ying, Trends Anal. Chem. 113 (2019) 1–12.
[7] Q. Wang, R. Li, Y. Zhao, et al., Talanta 219 (2020) 121255.
[8] G. Lang, J. Feng, B. Feng, et al., Chin. Chem. Lett. 35 (2024) 109113.
[9] E. Cheng, Y. Li, W. Yuan, et al., Chin. Chem. Lett. 35 (2024) 109386.
[10] F. Meng, X. Shi, Z. Yuan, et al., Sens. Actuators B 350 (2022) 130867.
[11] W. Qin, Z. Yuan, Y. Shen, et al., Chem. Eng. J. 431 (2022) 134280.
[12] G.A. Leith, A.M. Rice, B.J. Yarbrough, et al., Angew. Chem. Int. Ed. 132 (2020) 6056–6062.
[13] M.E. Ziebel, L.E. Darago, J.R. Long, J. Am. Chem. Soc. 140 (2018) 3040–3051.
[14] J. Suh, T.L. Tan, W. Zhao, et al., Nat. Commun. 9 (2018) 199.
[15] H. Chen, X. Liang, Z. You, et al., ACS Catal. 15 (2025) 1795–1806.
[16] G. Luo, E. Zhu, C. Shi, et al., Appl. Catal. B: Environ. 350 (2024) 123939.
[17] S. Ke, Y. Zhao, X. Min, et al., Int. J. Hydrogen Energy 105 (2025) 806–816.
[18] J. Yu, J. Li, C.Y. Xu, et al., Nano Energy 98 (2022) 107266.
[19] P. Guo, W. Chen, Y. Zhou, et al., Small 18 (2022) 2205158.
[20] Z.Y. Song, Z.W. Gao, Y.-Y. Li, et al., Anal. Chem. 95 (2023) 3666–3674.
[21] P. Jiang, H. Huang, J. Diao, et al., Appl. Catal. B: Environ. 258 (2019) 117965.
[22] W. Zhang, L. Yang, Z. Li, et al., Angew. Chem. Int. Ed. 63 (2024) e202400888.
[23] T. Li, L. Zhang, L. Zhang, et al., Adv. Funct. Mater. 34 (2024) 2309886.
[24] W. Pei, X. Ma, Y. Wu, et al., Appl. Catal. B: Environ. Energy 371 (2025) 125273.
[25] Z.Z. Shi, X. Wang, W.J. Kang, et al., ACS Appl. Energy Mater. 6 (2023) 10012–10019.
[26] X. Li, Y. Wang, J. Wang, et al., Adv. Mater. 32 (2020) 2003414.
[27] S. Shen, Z. Wang, Z. Lin, et al., Adv. Mater. 34 (2022) 2110631.
[28] Y. Zhao, Q. Xu, X. Zhou, et al., Ceram. Int. 49 (2023) 8259–8270.
[29] C. Xu, X. Yang, S. Li, et al., Inorg. Chem. Front. 10 (2023) 85–92.
[30] H.J. Niu, N. Ran, W. Zhou, et al., J. Am. Chem. Soc. 147 (2025) 2607–2615.
[31] Q.Y. Wang, H.R. Li, Z.Y. Zheng, et al., Microchem. J. 208 (2025) 112359.
[32] Z. Yang, J. Hui, W. Fan, et al., J. Energy Chem. 101 (2025) 156–162.
[33] W. Shangguan, G. Li, S. Gui, et al., Adv. Funct. Mater. 35 (2025) 2501285.
[34] C. Chen, P. Zhang, M. Wang, et al., ChemSusChem 13 (2020) 5067–5072.
[35] M. Wang, A. Peng, J. Jiang, et al., Chem. Eng. J. 433 (2022) 134567.
[36] Z. Zhong, P. Hansmann, Phys. Rev. B 93 (2016) 235116.
[37] R. Liu, C. Wang, Y. Yan, et al., ACS Catal. 14 (2024) 3955–3965.
[38] K. Yao, F. Pan, H. Liang, et al., Adv. Funct. Mater. 35 (2025) 2413639.
[39] Z. Nie, M. Chen, L. Zhang, et al., Chem. Eng. J. 463 (2023) 142411.
[40] C. Xuan, T. Shen, B. Hou, Chem. Eng. J. 479 (2024) 147723.
[41] X. Mo, X. Lu, S. Yang, et al., Environ. Sci. Technol. 59 (2025) 7357–7365.
[42] P.R. Jubu, E. Danladi, U. Ndeze, et al., Results Opt. 14 (2024) 100606.
[43] W. Ye, W. Zhang, X. Hu, et al., Sci. Total Environ. 732 (2020) 139245.
[44] Y. Wan, W. Wei, S. Ding, et al., Small 20 (2024) 2404689.
[45] M. Büchler, P. Schmuki, H. Böhni, Electrochim. Acta 43 (1998) 635–637.
[46] S.E. John, S.K. Mohapatra, M. Misra, Langmuir 25 (2009) 8240–8247.
[47] C.C. Naik, S. Mardolkar, A. Salker, Inorg. Chem. Commun. 168 (2024) 112886.
[48] A. Abram, A. Eršte, G. Dražić, et al., J. Mater. Sci.: Mater. Electron. 27 (2016) 10221–10225.
[49] J. Zhang, S. Cui, Y. Ding, et al., Biosens. Bioelectron. 112 (2018) 177–185.
[50] R.S. Nicholson, I. Shain, Anal. Chem. 36 (1964) 706–723.
[51] S.S. Li, J.H. Fang, L. Li, et al., Talanta 225 (2021) 122087.
[52] G. Tian, H. Xu, X. Wang, et al., Nano Energy 117 (2023) 108863.
[53] X. Wang, S. Huo, Y. Chen, et al., Adv. Funct. Mater. 35 (2025) 2506077.
[54] S.B. Khan, K. Akhtar, E.M. Bakhsh, et al., Appl. Surf. Sci. 492 (2019) 726–735.
[55] H.R. Li, H. Xu, Q.Y. Wang, et al., Talanta 285 (2025) 127360.
[56] X.Y. Xiao, Z.Y. Song, H. Xie, et al., Adv. Funct. Mater. 32 (2022) 2209283.
[57] C. Sandford, M.A. Edwards, K.J. Klunder, et al., Chem. Sci. 10 (2019) 6404–6422.
[58] K.J. Aoki, J. Chen, Y. Liu, et al., J. Electroanal. Chem. 856 (2020) 113609.
[59] A.J. Bard, L.R. Faulkner, Surf. Technol. 20 (1983) 91–92.
[60] X.L. Cheng, X. Xia, Q.Q. Xu, et al., Sens. Actuators B 348 (2021) 130692.
[61] X. Zhou, M. Luo, C. Xie, et al., Appl. Catal. B: Environ. 282 (2021) 119605.
[62] R. Balaji, T.T. Nguyen, Q.P. Ngo, et al., Adv. Funct. Mater. 34 (2024) 2410672.
[63] Y. Jiang, Y. Song, Z. Pan, et al., ACS Nano 12 (2018) 5011–5020.
[64] Z. Galus, J. Chem. Educ. 55 (1976) 5.
[65] B. Mohan, C.R. Girish, G. Jeppu, et al., Sci. Rep. 15 (2025) 31790.
[66] T. Zhang, Q. Lang, D. Yang, et al., Electrochim. Acta 106 (2013) 127–134.